

Enhanced third harmonic response of the PtTe_2 transition metal dichalcogenide

Leone Di Mauro Villari,^{1,*} Simone Grillo,^{2,3} Olivia Pulci,² Salvatore Macis,⁴ Stefano Lupi,⁴ and Andrea Marini^{1,5,†}

¹*Department of Physical and Chemical Sciences,*

University of L’Aquila, Via Vetoio, 67100 L’Aquila, Italy

²*Department of Physics, University of Rome Tor Vergata and INFN,*

Via della Ricerca Scientifica 1, 00133 Roma, Italy

³*Max Planck Institute for the Structure and Dynamics of Matter (MPSD) and*

Center for Free-Electron Laser Science (CFEL), 22761 Hamburg, Germany

⁴*Department of Physics, Sapienza University of Rome, Piazzale Aldo Moro, 00133 Roma, Italy*

⁵*CNR-SPIN, c/o Department of Physical and Chemical Sciences, Via Vetoio, Coppito (L’Aquila) 67100, Italy*

We investigate the third harmonic response of platinum ditelluride (PtTe_2), a Dirac semimetal belonging to the transition metal dichalcogenides class. Due to its topological properties, this material has drawn a lot of attention, particularly because it hosts type-II (super-critically tilted) Dirac fermions in the $\text{A} - \Gamma - \text{A}$ high symmetry direction. Adopting a low-energy model fitted directly from density functional theory band structure simulations, we calculate analytically the nonlinear conductivity. We observe that third-order optical nonlinearities are efficiently modulated by the cones tilting, which produces a significant enhancement of the nonlinear susceptibility. Our results, besides shedding light on topological transitions of platinum ditelluride, are relevant for future nanophotonic devices exploiting the tunable nonlinear properties of type-II Dirac fermions.

I. INTRODUCTION

Relativistic massless and massive fermions can be probed with high-energy physics experiments, but also appear as low-energy quasiparticle excitations in condensed matter systems, where their massless character is typically protected by crystal symmetries. In the twenty years since the discovery of graphene, Dirac and Weyl fermions (DFs-WFs) in two and three dimensions have been the subject of a remarkable amount of research in condensed matter physics [1–6]. The class of materials showing this low-energy behavior encompasses semimetals [7], transition metal dichalcogenides (TMDs) [8], and topological insulators [9]. Beyond standard (type-I) D-WFs new types of low-energy excitation were proposed [10, 11]. These quasiparticles, named type-II D-WFs, break Lorentz invariance, which is not a necessary constraint in condensed matter physics. Differently from conventional D-WFs which have standard point-like Fermi surfaces, type-II fermions emerge at the boundary between electron and hole pockets. As a consequence, instead of straight Dirac or Weyl cones (DCs-WCs), the low-energy spectrum is given by a strongly tilted cone. Dirac and Weyl type II quasiparticles are distinguished as in the standard case: the former is symmetry protected whilst the latter ought to break either inversion or time reversal symmetry. Shortly after their theoretical prediction, type-II fermions were experimentally observed in materials such as molybdenum ditelluride (MoTe_2) [12], tungsten disulfide (WSe_2) [13] and the platinum based PtX_2 class of TMDs ($\text{X}=\text{Te,Se,Bi}$) [14]. Beyond fundamental science type-II fermions are particularly relevant in the field of topological materials, in fact type-I

and type-II fermions can be regarded as two topological phases as the Fermi surface changes shape. The transition between the two types of fermions is called Lifshitz topological transition [10, 15]. More recently, the relation between topological and optical properties has started to attract attention [16–19]. In particular optical probing can be used to detect some signature of Lifshitz transitions [20–24] which notably can be induced by pressure [25]. Moreover it has been shown that the tilting of D-WCs significantly enhances the even harmonics response in non centrosymmetric media [26, 27].

In this paper we investigate the tensorial third harmonic response of platinum ditelluride (PtTe_2), a \mathcal{I} and \mathcal{T} symmetric type-II Dirac semimetal, which has been hitherto overlooked, while its linear response is well characterized [28]. Generally, crystalline third-order effects are difficult to be accounted for due to the significant complications in computing four-rank tensors. In the case of tilted fermions, such complications are even more pronounced due to Fermi velocity anisotropy (as it is for the PtX_2 class of materials). The reason behind these difficulties is that the Fermi surface has no more spherical symmetry but is rather elliptic or hyperbolic. For our calculation, we start from density functional theory electronic band structure simulations, to derive a minimal model for the low-energy bands around the nodal (type-II) points in the $\text{A} - \Gamma - \text{A}$ high symmetry direction. We then use finite temperature diagrammatic perturbation theory to evaluate the third harmonic response. This method simplifies the calculation of high order response functions and makes the inclusion of many-body effects considerably more straightforward. We find that PtTe_2 has a significantly strong THG signal in the terahertz (THz) regime along the tilting direction. In fact, the THG signal from a tilted Dirac fermion is one order of magnitude larger than the signal from an untilted one.

* leone.dimaurovillari@univaq.it

† andrea.marini@univaq.it

The paper is organised as follows. In section II we compute the minimal two band model starting from the DFT electronic band structure results. In section III, we develop the diagrammatic theory of the optical Dirac-Bloch equations. In section IV, we show the results for the third harmonic conductivity tensor.

II. LOW-ENERGY MODEL FROM DFT BAND STRUCTURE

In this section we briefly review the electronic properties of 1T-PtTe₂, which is a metal/semimetal in the bulk TMDs family. The crystal structure has trigonal symmetry and a three-atom unit cell, consisting of two Te atoms and one Pt atom.

The electronic band structure was calculated within DFT using the Quantum ESPRESSO package [29, 30], employing a norm-conserving, fully relativistic pseudopotential from the PseudoDojo repository [31] including spin-orbit coupling and semicore corrections, together with a generalized gradient approximation (GGA), according to Perdew, Burke and Ernzerhof (PBE) [32], for the exchange-correlation functional. A kinetic energy cutoff of 100 Ry and a 12×12×12 Monkhorst-Pack [33] k -point mesh were adopted after careful convergence tests. van der Waals interactions were taken into account using Grimme's PBE-DFT-D2 correction scheme. We then have derived the effective two-band model by fitting the lowest energy bands of the DFT band structure which we show in figure 1a, with the following model-Hamiltonian (see Fig. 1c)

$$H = a_0 \sigma_0 k_z + \sum_{i=(x,y,z)} a_i \sigma_i k_i, \quad (1)$$

where a_i are fitting coefficients, σ_i the Pauli matrices plus the identity (indicated with σ_0) and k_i the electron momentum. The fit gives the following values for the coefficients, $a_0 = -6.25$ eV Å, $a_x = 2.76$ eV Å, $a_y = -a_x$ and $a_z = -3.86$ eV Å. We can now rewrite the two bands Hamiltonian in a more convenient form by introducing the dimensionless tilting parameter $\tau = a_0/a_z$ and Fermi velocity anisotropy ($\eta_x = a_x/a_z$, $\eta_y = a_y/a_z$), hence

$$H = \eta_x \sigma_x q_x + \eta_y \sigma_y q_y + (\tau \sigma_0 + \sigma_z) q_z, \quad (2)$$

where the rescaled "momentum" $q_i = a_z k_i$ has the dimensions of an energy. With the Hamiltonian written in this form we can distinguish three cases $\tau < 1$ (tilted type-I DFs) $\tau = 1$ (critically tilted), $\tau > 1$ (supercritically tilted type-II DFs). In the case of PtTe₂, the tilting parameter is $\tau = 1.54$ hence it shows type-II DFs as we can clearly see in Figs. 1a,b.

The Hamiltonian in Eq. (2) can be easily diagonalized,

giving

$$\mathbf{u}_\mathbf{q}^\lambda = \frac{g_\mathbf{q}}{f_\mathbf{q} \sqrt{2w_{\mathbf{q},\lambda}}} \begin{pmatrix} \frac{f_\mathbf{q} w_{\mathbf{q},\lambda}}{g_\mathbf{q}} e^{-i\varphi_\mathbf{q}}, \\ 1 \end{pmatrix} \quad (3)$$

$$\varepsilon_{\mathbf{q},\lambda}^\xi = \xi q_z + \lambda \sqrt{\eta_x^2 q_x^2 + \eta_y^2 q_y^2 + q_z^2},$$

where $\lambda = \pm 1$ is the band index, $\xi = \pm 1$ is a pseudo-spin index which runs on the two type-II cones in the $\mathbf{A} - \Gamma - \mathbf{A}$ direction, while $g_\mathbf{q} = \sqrt{\eta_x^2 q_x^2 + \eta_y^2 q_y^2}$, $f_\mathbf{q} = \sqrt{\eta_x^2 q_x^2 + \eta_y^2 q_y^2 + q_z^2}$ and $w_{\mathbf{q},\lambda} = 1 + \lambda q_z/f_\mathbf{q}$.

III. FEYNMAN DIAGRAMMATIC EXPANSION OF THE BLOCH EQUATIONS

This section gives a short overview of the calculation of the nonlinear conductivity starting from the non-interacting semiconductor Bloch equations or optical Bloch equations (OBEs) in a mixed velocity/length gauge [34], which can be represented as a diagrammatic expansion. We choose a time-dependent frame which moves with the vector potential. Hence, the OBEs describe the evolution of the density matrix as (for the sake of conciseness, in this section we take $\hbar = c = e = 1$, unless specified)

$$i \frac{\partial}{\partial t} \rho_\mathbf{k} = [H_{\mathbf{k}-\mathbf{A}(t)}[\mathbf{E}(t)], \rho_\mathbf{k}], \quad (4)$$

where $\mathbf{A}(t)$ is the electromagnetic (EM) vector potential and $\mathbf{E}(t) = -\dot{\mathbf{A}}(t)$ is the electric field. Taking the expectation values over the bands eigenstates gives

$$i \frac{\partial}{\partial t} \rho_\mathbf{k}^{\lambda,\lambda'} = (\varepsilon_{\mathbf{k}+\mathbf{A}(t)}) \rho_\mathbf{k}^{\lambda,\lambda'} - \mathbf{E}(t) \cdot \mathcal{A}_\mathbf{k}^{\lambda,\lambda'} \rho_\mathbf{k}^{\lambda,\lambda'}, \quad (5)$$

where the matrix $\mathcal{A}_\mathbf{k}^{\lambda,\lambda'} = \langle \mathbf{u}_\mathbf{k}^\lambda | \nabla_\mathbf{k} | \mathbf{u}_\mathbf{k}^{\lambda'} \rangle$ is the non-abelian Berry connection and λ is a band index. This equation accounts for both the interband and intraband dynamics of the carriers. As we are interested in the nonlinear response, we express the full current as

$$\mathbf{J}(t) = \int \frac{d\mathbf{k}}{(2\pi)^3} \text{Tr} \left(\mathbf{j}_{\mathbf{k}-\mathbf{A}(t)}^{\lambda,\lambda'} \rho_\mathbf{k}^{\lambda,\lambda'}(t) \right), \quad (6)$$

where the $\mathbf{j}_\mathbf{k}^{\lambda,\lambda'} = \langle \mathbf{u}_\mathbf{k}^\lambda | \nabla_\mathbf{k} H_\mathbf{k} | \mathbf{u}_\mathbf{k}^{\lambda'} \rangle$ is the microscopic current operator. The current can be expanded perturbatively as [35]

$$\mathbf{J}(t) = \sum_n \int \frac{\Pi_{i=1}^n d\omega_i}{2\pi} \hat{\sigma}^{(n)}(\omega_\Sigma; \omega_1, \dots, \omega_n) e^{-i\omega_\Sigma t} \bigotimes_{i=1}^n \mathbf{E}_{\omega_i}, \quad (7)$$

where ω_i are external EM frequencies, $\omega_\Sigma = \omega_1 + \dots + \omega_n$, $\hat{\sigma}^{(n)}$ the n -th order conductivity tensor and $\mathbf{E}_{\omega_1} \otimes \mathbf{E}_{\omega_2} = E_{\omega_1}^a E_{\omega_2}^b$, with $a, b = (x, y, z)$ and \mathbf{E}_ω the electric field

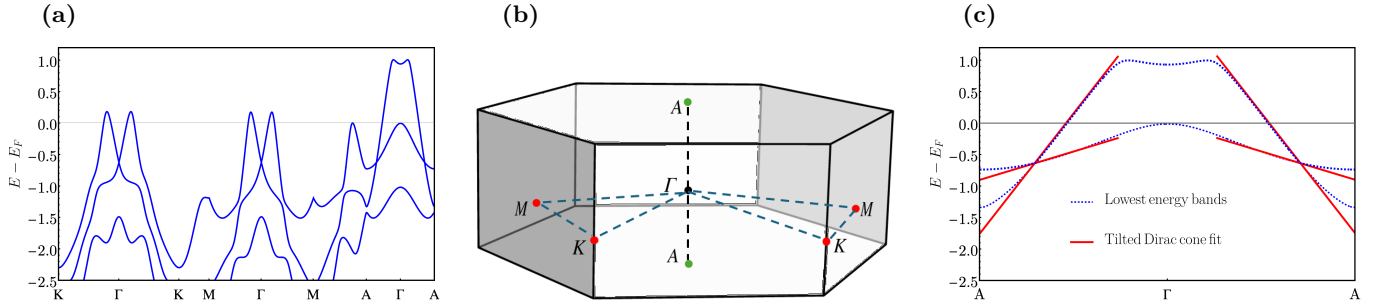


FIG. 1. (a) Bulk 1T-PtTe₂ electronic band structure, with SOC included, calculated with Grimme's PBE-DFT-D2 functionals, with high-symmetry directions in the hexagonal Brillouin zone at $k_z = 0.35(4)c^*$, where $c^* = 2\pi/c$ (we use Γ as a reference as $k_z = 0$). Energy rescaled with respect to the Fermi energy. It shows two type-I Dirac points in the K- Γ -K and M- Γ -M high symmetry direction, and two type-II points in the A- Γ -A direction. (b) Wave-vector path in the hexagonal Brillouin zone. (c) Lowest energy bands and fit with the low momentum expansion around the type-II nodes.

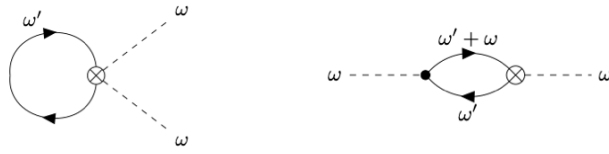


FIG. 2. First order conductivity diagrams.

Fourier transform. The nonlinear orders of the conductivity response functions can be found explicitly from the perturbative solution of the OBEs. The procedure is straightforward, but rather lengthy above all at high order. To this end a Feynman diagrammatic expansion is rather helpful. Depending on the gauge used and the response function considered, Feynman expansions have slightly different rules [36], even though they all give the same results if diagrams are evaluated carefully. We summarise here the rules for our specific case (from here we reintroduce physical units):

- draw electrons closed solid lines (loops) in all possible topologies allowed by the expansion order (n), i.e., with a maximum of $n + 1$ vertices. This gives 2^n diagrams at each order;
- associate a frequency to each solid or interaction line. Conserve frequency at each vertex;
- associate to each solid line a free electron propagator

$$G_\lambda(\mathbf{k}, \Omega_j) = \frac{1}{\Omega_j - \varepsilon_{\lambda, \mathbf{k}}},$$

where Ω_j are combinations of external photon frequencies and internal electron frequencies fixed by conservation of frequency;

- draw $n + 1$ external dashed photon lines to be "attached" to electron vertices;
- associate a frequency ω_i to each photon line attached to an input vertex and a frequency ω_Σ to photon lines attached to an output vertex;

- identify input and output interaction vertices, each diagram has one output vertex (with one output photon and a maximum of n input photons attached) and a maximum of n input vertices (with a maximum of n input photons attached);
- associate the appropriate current matrix element at each input and output vertex. An m -frequencies input vertex is given by

$$\mathcal{J}_{\lambda\lambda', \mathbf{k}}^{(m)\alpha_1, \dots, \alpha_m} = e^m \frac{\partial^{m-1}}{\partial k_{\alpha_1} \dots \partial k_{\alpha_{m-1}}} \left(\frac{\partial \varepsilon_{\mathbf{k}}^\lambda}{\partial k_{\alpha_m}} + m i \omega \mathcal{A}_{\mathbf{k}}^{\lambda\lambda'} \right),$$

while an l -frequency output vertex is given by

$$\mathcal{J}_{\lambda\lambda', \mathbf{k}}^{(l)\alpha_1, \dots, \alpha_l} = e^l \frac{\partial^{l-1}}{\partial k_{\alpha_1} \dots \partial k_{\alpha_{l-1}}} \langle u_{\mathbf{k}}^\lambda | \frac{\partial H_{\mathbf{k}}}{\partial k_{\alpha_l}} | u_{\mathbf{k}}^{\lambda'} \rangle,$$

with $m + l = n + 1$;

- integrate over the internal electron wavevector and frequencies with measures $\int d^d k / (2\pi)^d$ and $\int d\omega / (2\pi)$;
- multiply everything by a factor $\frac{i^n}{\hbar^{n+1} \prod_{i=1}^n \omega_i}$.

Equipped with these rules, we can draw all diagrams at each order and give the respective analytical expression. We consider the first order, as it is simpler and instructive, and the third-order, which is the one we are interested in. The second order (along with all even orders) is vanishing as the material is centrosymmetric.

The first diagram gives the intraband contribution to the conductivity while the second gives the interband contribution. According to the rules, such contributions can be represented as in Fig. 2 and their analytical expressions read

$$\sigma_{\alpha\beta}^{(1)}(\omega; \omega) = \frac{i}{\hbar^2 \omega} \int \frac{d^3 k}{(2\pi)^3} \int \frac{d\omega'}{2\pi} \left[\sum_{\lambda} J_{\lambda, \mathbf{k}}^{\alpha\beta} G_{\mathbf{k}}^{\lambda}(\omega') d\omega' + \sum_{\lambda\lambda'} \mathcal{J}_{\lambda\lambda', \mathbf{k}}^{\alpha} G_{\mathbf{k}}^{\lambda'}(\omega + \omega') J_{\lambda\lambda', \mathbf{k}}^{\beta} G_{\mathbf{k}}^{\lambda}(\omega') \right], \quad (8)$$

where the integration over internal frequencies can be performed using the standard technique of the Matsubara summation [37], while the integration over the momentum can be arbitrarily difficult and depend on the system under consideration. At third-order there are $2^3 = 8$ different diagrams which we show in Fig. 3. The analytical expression of the third-order conductivity is rather cumbersome and we refer to appendix A where we explain how to compute it explicitly.

IV. TOPOLOGICAL THIRD HARMONIC RESPONSE

In this section we show the result of the diagrammatic calculation for the third harmonic response, for which $\omega_1 = \omega_2 = \omega_3 = \omega$. PtTe₂ belongs to the D_{3d} symmetry group, hence the third-order conductivity tensor has 14 nonzero independent elements. Qualitatively their behaviour is rather similar, even though the enhancement due to the presence of type-II Dirac cones is more evident in the k_z -tilting direction. For this reason we shall show the results for the σ_{zzzz} and $\sigma_{xxzz} = \sigma_{yyzz}$ terms. The details of the diagrammatic calculations, for the bubble and triangle diagrams are shown in appendix A. Before detailing the THG, we review in figure 4a the first order response comparing type-I and type-II DCs [38]. We

can observe first that for type-I DCs $\sigma_{xx} = \sigma_{yy} = \sigma_{zz}$ while for type-II $\sigma_{xx} = \sigma_{yy} \neq \sigma_{zz}$. Secondly the resonances and analyticity properties are changed, for type-I the conductivity is zero before $\hbar\omega = 2\mu$ (with μ being the chemical potential) and is linear in energy for $\hbar\omega > 2\mu$, for the case of type-II to the onset of the interband transitions is at $\hbar\omega = 2\mu/(1 + \tau)$ and they show different quasi-linear behaviors for $2\mu/(\tau + 1) < \hbar\omega < 2\mu/(\tau - 1)$ and $\hbar\omega > 2\mu/(\tau - 1)$. The results are shown in Figs. 4b-d. In Figs. 4b,c we show the σ_{zzzz} and σ_{xxzz} for the THG process, both for a type-I and a type-II DC with chemical potential $\mu = 0.08$ eV. We can see that type-II cones show a significantly larger signal for both the tensor terms, at low-energy (with respect to the nodal point). This is due to the fact that more k -states become available for transitions at low-energy, on the contrary at higher energy less states are available in the tilted case (this is also clearly visible in the first-order response). As we can observe from Fig. 4d, the THG signal is enhanced by 4.5 times for the $zzzz$ -tensor element and by 8-times for the $xxzz$ -tensor element and is independent from the doping (in the considered range and within the validity of the low-energy model). Considering that third-order effects are generally very low, such an increase is remarkable and makes Pt based TMDs excellent platforms for nonlinear optical frequency conversion, as recently confirmed experimentally [39]. Moreover, as it can be seen from Figs. 4a and b, the resonance structure of the nonlinear response is affected by the topological transition (i.e. the presence of type-II nodes). The expressions of the real part of THG conductivity can be compactly written as

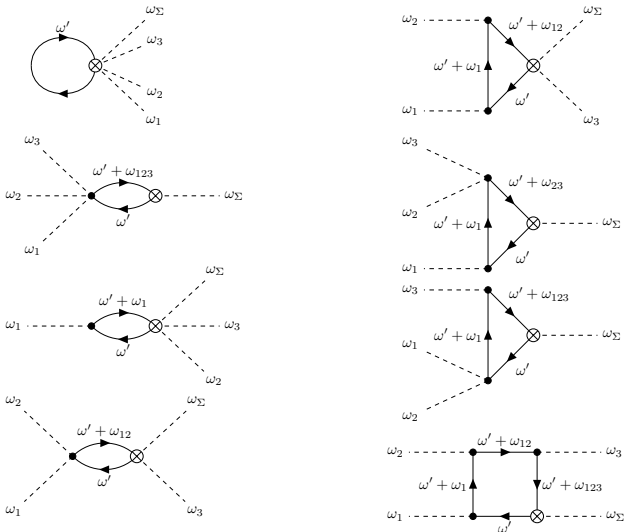


FIG. 3. Third-order conductivity diagrams.

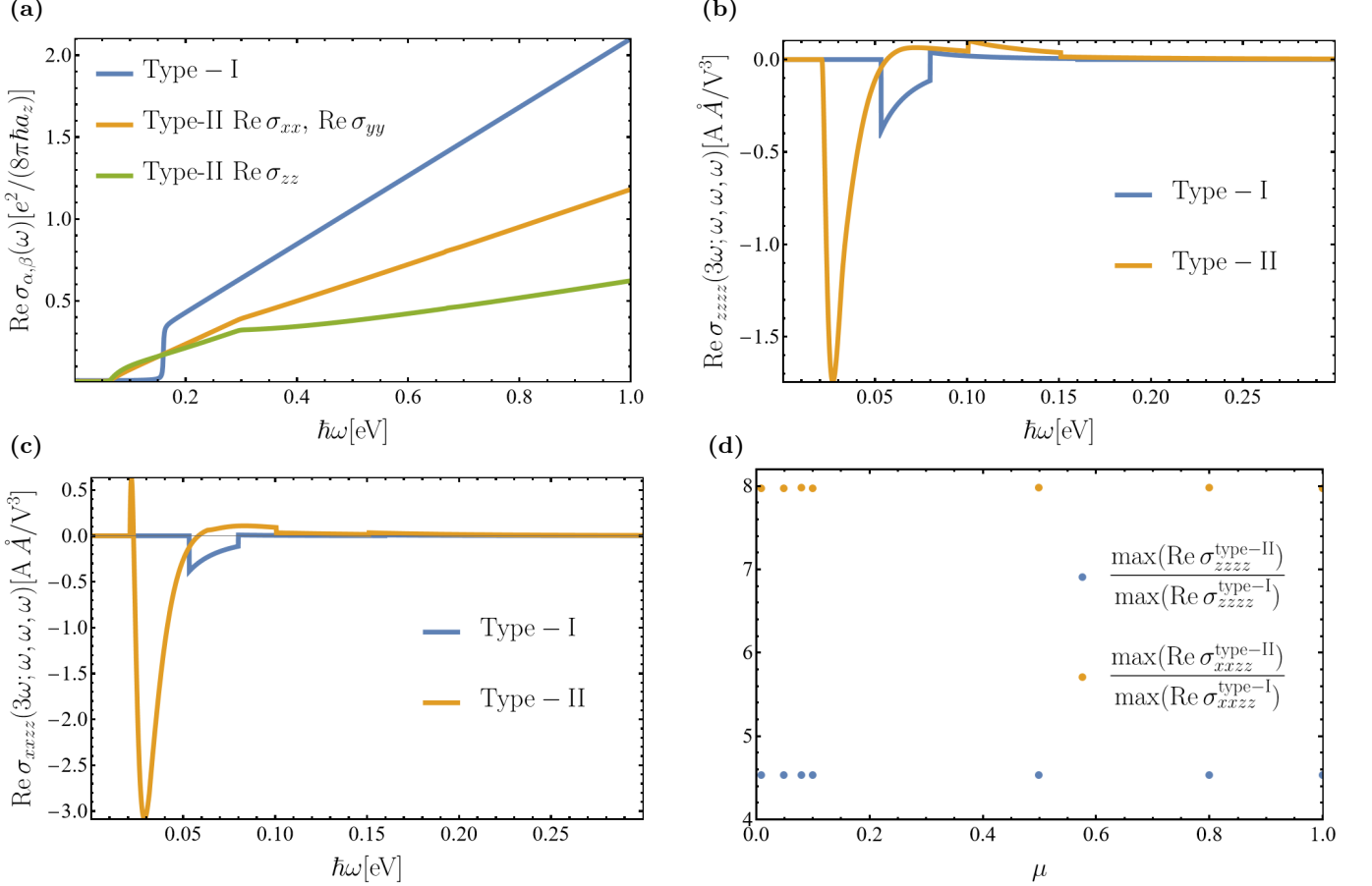


FIG. 4. Real part of the first order and THG nonlinear conductivity tensor at $T = 0$. (a) first order response for PtTe_2 (type-II, $xx = yy$ and zz -directions) and an ideal massless type-I Dirac cone ($xx = yy = zz$). (b) $\sigma_{zzzz}(3\omega; \omega, \omega, \omega)$ and (c) $\sigma_{xxzz}(3\omega; \omega, \omega, \omega)$ for PtTe_2 (type-II) and an ideal massless type-I Dirac cone. (d) THG enhancement, defined as the ratio between the maximum conductivity of the type-II and type-I nodes, as a function of chemical potential.

$$\begin{aligned} \text{Re } \sigma_{\alpha,\beta,\gamma,\delta}^{\text{tyI}}(3\omega; \omega, \omega, \omega) &= f_{\alpha,\beta,\gamma,\delta}^{(1)}(\omega) \Theta\left(\frac{2}{3}\mu - \hbar\omega\right) + f_{\alpha,\beta,\gamma,\delta}^{(2)}(\omega) \Theta(\mu - \hbar\omega) + f_{\alpha,\beta,\gamma,\delta}^{(3)}(\omega) \Theta(2\mu - \hbar\omega) \\ \text{Re } \sigma_{\alpha,\beta,\gamma,\delta}^{\text{tyII}}(3\omega; \omega, \omega, \omega) &= \sum_{m=\pm 1} \left[g_{\alpha,\beta,\gamma,\delta}^{(1),m}(\omega, \tau) \Theta\left(\frac{2\mu}{3(\tau+m)} - \hbar\omega\right) + g_{\alpha,\beta,\gamma,\delta}^{(2),m}(\omega, \tau) \Theta\left(\frac{\mu}{\tau+m} - \hbar\omega\right) + g_{\alpha,\beta,\gamma,\delta}^{(3),m}(\omega, \tau) \Theta\left(\frac{2\mu}{\tau+m} - \hbar\omega\right) \right] \end{aligned} \quad (9)$$

The multiplying functions (f, g) are in general given by rather complicated integrals which are read off from the diagrammatic expansion (see appendix A). The presence of the tilting modifies the position of the resonances in energy space, which are given by the arguments of the Heaviside Θ -functions. In the case of type-I DCs (blue curve in Fig. 4a,b) there are three resonances, located at $\hbar\omega = (2/3\mu, \mu, 2\mu)$ while for the case of type-II, due to tilting, there are six resonances $\hbar\omega = \{2\mu/[3(\tau \pm 1)], \mu/(\tau \pm 1), 2\mu/(\tau \pm 1)\}$. Thanks to the matching between Heaviside functions, which is tuned by the tilting parameter τ , the response of PtTe_2 type-II DCs is smooth in the interval $2\mu/[3(\tau + 1) \leq \hbar\omega < 2\mu/[3(\tau - 1)]$. It shows, instead, Θ -singularities at $\hbar\omega = \{2\mu/[3(\tau + 1)], 2\mu/(\tau + 1), \mu/(\tau + 1)\}$.

V. CONCLUSION

In this paper we studied the nonlinear optical response of the PtX_2 class of TMDs. We have focussed on PtTe_2 , but our calculations holds for all materials of the same class as they share the same electronic and symmetry properties. In section II we presented DFT calculation of the electronic band structure from which we derived a low-energy two-band model in the $\text{A} - \Gamma - \text{A}$ high symmetry direction, where it hosts two symmetric type-II Dirac fermions. We then analytically diagonalized the two bands Hamiltonian. In section III we derived a Feynman diagrammatic expansion of the OBEs and listed the rules for the drawing of the diagrams at each order. Finally, in section IV we presented the results of the fully analytical calculation of the third-order diagrams. We

show a significant enhancement (up to 8 times) of the third harmonic response due to the presence of the type-II Dirac cones together with a tilted induced shifting of the resonances and a change in the analyticity properties of the response function. This suggests that Pt based TMDs are an excellent platform for nonlinear optical interactions and that nonlinear spectroscopy may be employed to get indirect evidences of topological transitions. As a conclusive remark we note that we have limited our study to the single electron approximation i.e. we have neglected many-body interactions. From a qualitative point of view this approach is rather accurate at least far from excitonic resonances [40]. In perspective, to account for quantitative corrections the formalism employed in this paper may be extended to include many body effects.

Appendix A: Explicit calculation of some diagrams

In this appendix we show the explicit calculation of third harmonic diagrams. We focus on the real part, the imaginary one can either be calculated in a similar fashion or numerically using the Kramers-Kronig relations. Let us start with the bubble diagrams, the first one describes the intraband transitions and only contributes to the imaginary part. While the remaining three bubble diagrams contribute to both the real and imaginary part. The sum of these three diagrams, after performing the Matsubara summation, reads

$$B_{\alpha\beta\gamma\delta}(3\epsilon, \epsilon, \epsilon, \epsilon) = -\frac{i}{2\hbar\epsilon^3(2\pi)^3} \sum_{n=1}^3 \sum_{\{\lambda_i\}} \int d\mathbf{k} \mathcal{B}_{\lambda_1, \lambda_2, \mathbf{k}}^{n, \alpha\beta\gamma\delta} \frac{n_{\mathbf{k}}^{\lambda_1, \lambda_2}}{n\epsilon^+ - \varepsilon_{\mathbf{k}}^{\lambda_1, \lambda_2}}, \quad (\text{A1})$$

where $\epsilon = \hbar\omega$ and $\epsilon^+ = \hbar\omega + i\gamma$, $\mathcal{B}_{n, \lambda_1, \lambda_2, \mathbf{k}}^{n, \alpha\beta\gamma\delta}$ is the vertex function for each bubble diagram. Using a Pauli-Villars-like regularization we can separate the integrand into two contributions

$$B_{\alpha\beta\gamma\delta}(3\epsilon, \epsilon, \epsilon, \epsilon) = -\frac{ia_z}{\hbar\epsilon^3(2\pi)^3\eta^2} \sum_{n=1}^3 \int_{4\pi} d\Omega \tilde{\mathcal{B}}_{1-1, \theta, \phi}^{n, \alpha\beta\gamma\delta} \int_0^\infty dq \left[\frac{2}{n} \left(\frac{1}{n\epsilon^+ - 2q} - \frac{1}{n\epsilon^+ + 2q} \right) + \frac{1}{q} \right] n_{q, \theta}^{1, -1}, \quad (\text{A2})$$

where we have used elliptical coordinates ($q_x = q/\eta \cos \phi \sin \theta$, $q_y = q/\eta \sin \phi \sin \theta$, $q_z = q/\eta_z \cos \theta$) with $q_i = a_z k_i$ and $\eta = \eta_x = -\eta_y$, we have defined the rescaled vertex function as $\mathcal{B}_{1-1, \theta, \phi}^{n, \alpha\beta\gamma\delta} = \epsilon/q^3 \tilde{\mathcal{B}}_{1-1, \theta, \phi}^{n, \alpha\beta\gamma\delta}$ and summed over the band index λ_i . It can be shown that in the limit $\tau = 0$ (massive Dirac fermions), the second term has the well-known logarithmic UV-divergence for each diagram, which cancels out under resummation of the three bubble diagrams. For tilted cones, instead, while having also a

diverging contribution (vanishing under resummation) it also gives a finite imaginary contribution. Using now the Sokhotski-Plemelj formula over the real line

$$\frac{1}{x \pm i\gamma} = \mp i\pi\delta(x) + \mathcal{P}\left[\frac{1}{x}\right] \quad (\text{A3})$$

where $\mathcal{P}[\cdot]$ indicates the Cauchy principal value, we can isolate the real part of the bubble conductivity

$$\begin{aligned} \text{Re}[B_{\alpha\beta\gamma\delta}(3\epsilon, \epsilon, \epsilon, \epsilon)] = & -\frac{\pi a_z}{\hbar\epsilon^3(2\pi)^3\eta^2} \sum_{n=1}^3 \int_{4\pi} d\Omega \tilde{\mathcal{B}}_{1-1, \theta, \phi}^{n, \alpha\beta\gamma\delta} \\ & \int_0^\infty dq \left[\frac{2}{n} \left(\delta(n\epsilon^+ - 2q) - \delta(n\epsilon^+ + 2q) \right) \right] n_{q, \theta}^{1, -1}, \end{aligned} \quad (\text{A4})$$

as stated in the main text this expression can be computed analytically for every non-zero tensor element even for non-zero temperature, however the expressions are cumbersome and in general not particularly instructive especially for finite temperature. To show the main feature of the result we report explicitly the $zzzz$ -element for $T = 0$ whose main qualitative characteristics hold for every tensor element. We get

$$\begin{aligned} \text{Re}[B_{zzzz}(3\epsilon, \epsilon, \epsilon, \epsilon)] = & \frac{a_z}{8\pi\hbar\eta^2\epsilon^3} \sum_{n=1}^3 \int_{-1}^1 dw \tilde{\mathcal{B}}_{1-1, w}^{n, zzzz} \\ & \frac{1}{n} [\Theta(n\frac{\epsilon}{2}(1 + \tau w) - \mu) - \Theta(-n\frac{\epsilon}{2}(1 - \tau w) - \mu)], \end{aligned} \quad (\text{A5})$$

where $w = \cos \theta$, μ the chemical potential and $\Theta(x)$ the Heaviside step function. The rescaled vertex functions for the three diagrams are given by

$$\begin{aligned} \tilde{\mathcal{B}}_{1-1, w}^{1, zzzz} &= (1 - w^2)(6w^2 - 2)/4 \\ \tilde{\mathcal{B}}_{1-1, w}^{2, zzzz} &= 4(1 - w^2)w^2, \\ \tilde{\mathcal{B}}_{1-1, w}^{3, zzzz} &= 3(1 - w^2)(4w^2 - 1), \end{aligned} \quad (\text{A6})$$

hence we have reduced the seemingly complicated integral in equation A2 to a sum of polynomial integrals. The analytical result for the real part of the THG bubble conductivity in the $zzzz$ -direction at $T = 0$ is given by

$$\begin{aligned} \text{Re}[B_{zzzz}(3\epsilon, \epsilon, \epsilon, \epsilon)] = & \frac{e^4 a_z}{8\pi\hbar\eta^2\epsilon^3} \\ & \left[b_-^1(\epsilon, \tau) \Theta\left(\hbar\epsilon - \frac{2\mu}{3(1 + \tau)}\right) + b_-^2(\epsilon, \tau) \Theta\left(\hbar\epsilon - \frac{\mu}{1 + \tau}\right) + \right. \\ & b_-^3(\epsilon, \tau) \Theta\left(\hbar\epsilon - \frac{2\mu}{1 + \tau}\right) + b_+^1(\epsilon, \tau) \Theta\left(\hbar\epsilon - \frac{2\mu}{3(\tau - 1)}\right) + \\ & b_+^2(\epsilon, \tau) \Theta\left(\hbar\epsilon - \frac{\mu}{\tau - 1}\right) + b_+^3(\epsilon, \tau) \Theta\left(\hbar\epsilon - \frac{2\mu}{\tau - 1}\right) \left. \right], \end{aligned} \quad (\text{A7})$$

the $b_\pm^i(\epsilon, \tau)$ functions are defined as

$$\begin{aligned}
b_{\pm}^1(\epsilon, \tau) &= -\frac{2}{1215\epsilon^5} (405\tau^4\epsilon^4(2\mu \pm 3\epsilon) - 75\tau^2\epsilon^2(2\mu \pm 3\epsilon)^3 + 4(2\mu \pm 3\epsilon)^5 + 162\tau^5\epsilon^5), \\
b_{\pm}^2(\epsilon, \tau) &= \frac{1}{15\epsilon^5} (4\tau^5\epsilon^5 + 15\tau^4\epsilon^4(2\mu \pm \epsilon) - 20\tau^2\epsilon^2(2\mu \pm \epsilon)^3 + 9(2\mu \pm \epsilon)^5), \\
b_{\pm}^3(\epsilon, \tau) &= \frac{4}{15\epsilon^5} (2\tau^5\epsilon^5 + 5\tau^2\epsilon^2(\mu \pm \epsilon)^3 - 3(\mu \pm \epsilon)^5)
\end{aligned} \tag{A8}$$

The triangle conductivity diagrams are instead given by the following expression

$$\begin{aligned}
T_{\alpha, \beta, \gamma, \delta}(3\epsilon, \epsilon, \epsilon, \epsilon) &= -\frac{i}{\hbar(2\pi\epsilon)^3} \sum_{\{\lambda_i\}} \int d\mathbf{k} d\epsilon' \left[G(\epsilon') \mathcal{J}_{\lambda_1, \lambda_2, \mathbf{k}}^{\alpha} G(\epsilon' + \epsilon_1) \mathcal{J}_{\lambda_2, \lambda_3, \mathbf{k}}^{\beta} G(\epsilon' + \epsilon_{1,2}) J_{\lambda_3, \lambda_1, \mathbf{k}}^{\gamma; \delta} + \right. \\
&\quad \frac{1}{2!} G(\epsilon') \mathcal{J}_{\lambda_1, \lambda_2, \mathbf{k}}^{\alpha} G(\epsilon' + \epsilon_1) \mathcal{J}_{\lambda_2, \lambda_3, \mathbf{k}}^{\beta; \gamma} G(\epsilon' + \epsilon_{123}) J_{\lambda_3, \lambda_1, \mathbf{k}}^{\delta} + \\
&\quad \left. \frac{1}{2!} G(\epsilon') \mathcal{J}_{\lambda_1, \lambda_2, \mathbf{k}}^{\alpha; \beta} G(\epsilon' + \epsilon_{1,2}) \mathcal{J}_{\lambda_2, \lambda_3, \mathbf{k}}^{\gamma} G(\epsilon' + \epsilon_{123}) J_{\lambda_3, \lambda_1, \mathbf{k}}^{\delta} \right].
\end{aligned} \tag{A9}$$

Performing again the Matsubara summation we get

$$\begin{aligned}
T_{\alpha\beta\gamma\delta}(3\epsilon, \epsilon, \epsilon, \epsilon) &= -\frac{i}{\hbar(2\pi\epsilon)^3} \sum_{\{\lambda_i\}} \int d\mathbf{k} \left[\frac{\mathcal{T}_{\lambda_1 \lambda_2 \lambda_3, \mathbf{k}}^{1, \alpha, \beta, \gamma, \delta}}{2\epsilon^+ - \varepsilon_{\mathbf{k}}^{\lambda_3 \lambda_1}} \left(\frac{n_{\mathbf{k}}^{\lambda_1 \lambda_2}}{\epsilon^+ - \varepsilon_{\mathbf{k}}^{\lambda_2 \lambda_1}} + \frac{n_{\mathbf{k}}^{\lambda_3 \lambda_2}}{\epsilon^+ - \varepsilon_{\mathbf{k}}^{\lambda_3 \lambda_2}} \right) + \right. \\
&\quad \left. \frac{\mathcal{T}_{\lambda_1 \lambda_2 \lambda_3, \mathbf{k}}^{2, \alpha, \beta, \gamma, \delta}}{3\epsilon^+ - \varepsilon_{\mathbf{k}}^{\lambda_3 \lambda_1}} \left(\frac{n_{\mathbf{k}}^{\lambda_1 \lambda_2}}{\epsilon^+ - \varepsilon_{\mathbf{k}}^{\lambda_2 \lambda_1}} + \frac{n_{\mathbf{k}}^{\lambda_3 \lambda_2}}{2\epsilon^+ - \varepsilon_{\mathbf{k}}^{\lambda_2 \lambda_1}} \right) + \frac{\mathcal{T}_{\lambda_1 \lambda_2 \lambda_3, \mathbf{k}}^{3, \alpha, \beta, \gamma, \delta}}{3\epsilon^+ - \varepsilon_{\mathbf{k}}^{\lambda_3 \lambda_1}} \left(\frac{n_{\mathbf{k}}^{\lambda_1 \lambda_2}}{2\epsilon^+ - \varepsilon_{\mathbf{k}}^{\lambda_2 \lambda_1}} + \frac{n_{\mathbf{k}}^{\lambda_3 \lambda_2}}{\epsilon^+ - \varepsilon_{\mathbf{k}}^{\lambda_3 \lambda_2}} \right) \right],
\end{aligned} \tag{A10}$$

where again $\mathcal{T}_{\{\lambda_i\}, \mathbf{k}}^{i, \alpha, \beta, \gamma, \delta}$ are the vertex functions. Akin to the bubble diagram case, the calculation of the real part can be reduced to a polynomial integral; hence, it is a moot exercise to repeat the calculations. We obtain an analog resonant structure for the real part of the $zzzz$ -term at

zero temperature,

$$\begin{aligned}
\text{Re}[T_{zzzz}(3\epsilon, \epsilon, \epsilon, \epsilon)] &= \frac{e^4 a_z}{8\pi\hbar\eta^2\epsilon^3} \\
&\quad \left[t_{-}^1(\epsilon, \tau) \Theta\left(\hbar\epsilon - \frac{2\mu}{1+\tau}\right) + t_{-}^2(\epsilon, \tau) \Theta\left(\hbar\epsilon - \frac{\mu}{1+\tau}\right) + \right. \\
&\quad t_{-}^3(\epsilon, \tau) \Theta\left(\hbar\epsilon - \frac{2\mu}{3(1+\tau)}\right) + t_{+}^1(\epsilon, \tau) \Theta\left(\hbar\epsilon - \frac{2\mu}{\tau-1}\right) + \\
&\quad \left. t_{+}^2(\epsilon, \tau) \Theta\left(\hbar\epsilon - \frac{\mu}{\tau-1}\right) + t_{+}^3(\epsilon, \tau) \Theta\left(\hbar\epsilon - \frac{2\mu}{3(\tau-1)}\right) \right],
\end{aligned} \tag{A11}$$

where the $t_{\pm}^i(\epsilon, \tau)$ functions are defined as

$$\begin{aligned}
t_{\mp}^1(\epsilon, \tau) &= \int_{\gamma_{\mp}^{(1)}} dw [2\tilde{\mathcal{T}}_{-1, 1, -1}^{1, zzzz}(w, \tau) + \tilde{\mathcal{T}}_{1, -1, 1}^{2, zzzz}(w, \tau) - \tilde{\mathcal{T}}_{-1, 1, -1}^{3, zzzz}(w, \tau) + \tilde{\mathcal{T}}_{-1, -1, 1}^{1, zzzz}(w, \tau) + \\
&\quad + \tilde{\mathcal{T}}_{-1, -1, 1}^{2, zzzz}(w, \tau) + \tilde{\mathcal{T}}_{-1, 1, 1}^{1, zzzz}(w, \tau) + \tilde{\mathcal{T}}_{-1, 1, 1}^{3, zzzz}(w, \tau)] \\
t_{\mp}^2(\epsilon, \tau) &= \frac{1}{2} \int_{\gamma_{\mp}^{(2)}} dw [-2\tilde{\mathcal{T}}_{-1, 1, -1}^{2, zzzz}(w, \tau) + 2\tilde{\mathcal{T}}_{1, -1, 1}^{3, zzzz}(w, \tau) - \tilde{\mathcal{T}}_{-1, -1, 1}^{1, zzzz}(w, \tau) + \\
&\quad + \tilde{\mathcal{T}}_{-1, -1, 1}^{3, zzzz}(w, \tau) - \tilde{\mathcal{T}}_{-1, 1, 1}^{1, zzzz}(w, \tau) + \tilde{\mathcal{T}}_{-1, 1, 1}^{2, zzzz}(w, \tau)] \\
t_{\mp}^3(\epsilon, \tau) &= \int_{\gamma_{\mp}^{(3)}} dw [\tilde{\mathcal{T}}_{-1, -1, 1}^{2, zzzz}(w, \tau) + \tilde{\mathcal{T}}_{-1, -1, 1}^{3, zzzz}(w, \tau) - \tilde{\mathcal{T}}_{-1, 1, 1}^{2, zzzz}(w, \tau) + \tilde{\mathcal{T}}_{-1, 1, 1}^{3, zzzz}(w, \tau)]
\end{aligned} \tag{A12}$$

where the γ -intervals are given by $\gamma_{\mp}^{(n)} = [-(2\mu - n\epsilon)/(n(\tau + 1)), 1], [(2\mu - n\epsilon)/(n(\tau + 1)), (2\mu + n\epsilon)/(n(\tau + 1))]$ and

the rescaled vertex functions reads

$$\tilde{\mathcal{T}}_{1,-1,1}^{n,zzzz}(w, \tau) = \left\{ \frac{1}{4} (1 - w^2)^2, -2w (1 - w^2) (\tau + w), -w (1 - w^2) (\tau + w) \right\}, \quad (\text{A13})$$

$$\tilde{\mathcal{T}}_{-1,1,-1}^{n,zzzz}(w, \tau) = \left\{ \frac{1}{4} (1 - w^2)^2, w (1 - w^2) (\tau + w), 2w (1 - w^2) (\tau + w) \right\}, \quad (\text{A14})$$

$$\tilde{\mathcal{T}}_{-1,-1,1}^{n,zzzz}(w, \tau) = \left\{ 2w (1 - w^2) (w - \tau), \frac{1}{2} (1 - w^2)^2, 4w (1 - w^2) (w - \tau) \right\}, \quad (\text{A15})$$

$$\tilde{\mathcal{T}}_{-1,1,1}^{n,zzzz}(w, \tau) = \left\{ w (1 - w^2) (\tau + w), 6w (1 - w^2) (w - \tau), \frac{1}{4} (1 - w^2)^2 \right\}, \quad (\text{A16})$$

where we only considered the terms contributing to the

positive resonances. The calculation of the square diagram is done in the same way.

[1] K. S. Novoselov, A. K. Geim, S. V. Morozov, Y. Z. D. Jiang, S. V. Dubonos, I. V. Grigorieva, and A. A. Firsov, Electric field effect in atomically thin carbon films, *Science* **306**, 666 (2004).

[2] A. H. Castro Neto, F. Guinea, N. M. R. Peres, K. S. Novoselov, and A. K. Geim, The electronic properties of graphene, *Rev. Mod. Phys.* **81**, 109 (2009).

[3] R. R. Nair, P. Blake, A. N. Grigorenko, K. S. Novoselov, T. J. Booth, T. Stauber, N. M. R. Peres, and A. K. Geim, Fine structure constant defines visual transparency of graphene, *Science* **320**, 1308 (2008).

[4] T. O. Wehling, A. Black-Shaffer, and A. V. Balatsky, Dirac materials, *Advances in Physics* **63**, 1 (2013).

[5] Y. S. Z. Wang, X.-Q. Chen, C. Franchini, X. D. G. Xu, H. Weng, and Z. Fang, Dirac semimetal and topological phase transitions in A_3Bi ($A=Na, K, Rb$), *Phys. Rev. B* **85**, 195320 (2012).

[6] Z. Wang, H. Weng, Q. Wu, X. Dai, and Z. Fang, Three-dimensional dirac semimetal and quantum transport in Cd_3As_2 , *Phys. Rev. B* **88**, 125427 (2013).

[7] A. Thakur, K. Sadhukhan, and A. Agarwal, Dynamic current-current susceptibility in three-dimensional dirac and weyl semimetals, *Phys. Rev. B* **97**, 035403 (2018).

[8] M. Xu, T. Liang, M. Shi, and H. Chen, Graphene-like two-dimensional materials, *Chem. Rev.* **113**, 3766 (2013).

[9] M. Z. Hasan and C. L. Kane, Colloquium: Topological insulators, *Rev. Mod. Phys.* **82**, 3045 (2010).

[10] A. A. Soluyanov, D. Gresch, Z. Wang, Q. Wu, M. Troyer, X. Dai, and B. A. Bernevig, Type-II Weyl semimetals, *Nature* **527** (2015).

[11] H. Huang, S. Zhou, and W. Duan, Type-II Dirac fermions in the $ptse_2$ class of transition metal dichalcogenides, *Phys. Rev. B* **94**, 121117 (2016).

[12] K. Deng, G. Wan, G. Deng, P. Wan, P. Deng, K. Zhang, S. Ding, E. Wang, M. Yan, H. Huang, H. Zhang, Z. Xu, J. Denlinger, A. Fedorov, H. Yang, W. Duan, H. Yao, Y. Wu, S. Fan, H. Zhang, X. Chen, and S. Zhou, Experimental observation of topological fermi arcs in type-II weyl semimetal $MoTe_2$, *Nat. Phys.* **12**, 1105–1110 (2016).

[13] C. Wang, Y. Zhang, J. Huang, S. Nie, G. Liu, A. Liang, Y. Zhang, B. Shen, J. Liu, C. Hu, Y. Ding, D. Liu, Y. Hu, S. He, L. Zhao, L. Yu, J. Hu, J. Wei, Z. Mao, Y. Shi, X. Jia, F. Zhang, S. Zhang, F. Yang, Z. Wang, Q. Peng, H. Weng, X. Dai, Z. Fang, Z. Xu, C. Chen, and X. J. Zhou, Observation of Fermi arc and its connection with bulk states in the candidate type-II Weyl semimetal wte_2 , *Phys. Rev. B* **94**, 241119 (2016).

[14] M. Yan, H. Huang, K. Zhang, E. Wang, W. Yao, K. Deng, G. Wan, H. Zhang, M. Arita, H. Yang, Z. Sun, H. Yao, Y. Wu, S. Fan, W. Duan, and S. Zhou, Lorentz-violating type-II dirac fermions in transition metal dichalcogenide $PtTe_2$, *Nature Communications* **8**, 257 (2017).

[15] G. E. Volovik and K. Zhang, Lifshitz transitions, type-II Dirac and Weyl fermions, event horizon and all that, *Journal of Low Temperature Physics* **189**, 276 (2017).

[16] D. N. Carvalho, F. Biancalana, and A. Marini, Nonlinear optical effects of opening a gap in graphene, *Phys. Rev. B* **97**, 195123 (2018).

[17] T. N. Ikeda, High-order nonlinear optical response of a twisted bilayer graphene, *Phys. Rev. Research* **2**, 032015 (2020).

[18] J. W. Zuber and C. Zhang, Nonlinear optical response of twisted bilayer graphene, *Phys. Rev. B* **103**, 245417 (2021).

[19] L. Di Mauro Villari and A. Principi, Optotwistronics of bilayer graphene, *Physical Review B* **106**, 035401 (2022).

[20] C.-Y. Tan, J.-T. Hou, C.-X. Yan, H. Guo, and H.-R. Chang, Signatures of lifshitz transition in the optical conductivity of two-dimensional tilted dirac materials, *Phys. Rev. B* **106**, 165404 (2022).

[21] E. J. Sie, C. M. Nyby, C. D. Pemmaraju, S. J. Park, X. Shen, *et al.*, An ultrafast symmetry switch in a weyl semimetal, *Nature* **565**, 61 (2019).

[22] C. Heide, Y. Kobayashi, D. R. Baykusheva, D. Jain, J. A. Sobota, M. Hashimoto, P. S. Kirchmann, S. Oh, T. F. Heinz, D. A. Reis, and S. Ghimire, Probing topological phase transitions using high-harmonic generation, *Nature Photonics* **16**, 620 (2022).

[23] D. Bauer, Optically sensing topological phase transitions, *Nature Photonics* **16**, 614 (2022).

[24] T. Morimoto and N. Nagaosa, Topological nature of nonlinear optical effects in solids, *Science Advances* **2**, e1501524 (2016).

[25] P. Di Pietro, M. Mitrano, S. Caramazza, F. Capitani,

S. Lupi, P. Postorino, F. Ripanti, B. Joseph, N. Ehlen, A. Grüneis, A. Sanna, G. Profeta, P. Dore, and A. Perucchi, Emergent Dirac carriers across a pressure-induced Lifshitz transition in black phosphorus, *Phys. Rev. B* **98**, 165111 (2018).

[26] Y. Tamashevich, L. Di Mauro Villari, and M. Ornigotti, Nonlinear optical response of type-ii weyl fermions in two dimensions, *Physical Review B* **105**, 195102 (2022).

[27] Y. Tamashevich, L. Di Mauro Villari, and M. Ornigotti, Two-dimensional weyl materials in the presence of constant magnetic fields, *Physical Review B* **107**, 245425 (2023).

[28] S. Macis, A. D’Arco, L. Mosesso, M. C. Paolozzi, S. Tofani, L. Tomarchio, P. P. Tummala, S. Ghomi, V. Stopponi, E. Bonaventura, C. Massetti, D. Codegoni, A. Serafini, P. Targa, M. Zacchigna, A. Lamperti, C. Martella, A. Molle, and S. Lupi, Terahertz and infrared plasmon polaritons in PtTe₂ type-ii dirac topological semimetal, *Advanced Materials* **36**, 2400554 (2024), article e2400554.

[29] P. Giannozzi, S. Baroni, N. Bonini, M. Calandra, R. Car, C. Cavazzoni, D. Ceresoli, G. L. Chiarotti, M. Cococcioni, I. Dabo, *et al.*, QUANTUM ESPRESSO: a modular and open-source software project for quantum simulations of materials, *Journal of Physics: Condensed Matter* **21**, 395502 (2009).

[30] P. Giannozzi, O. Andreussi, T. Brumme, O. Bunau, M. B. Nardelli, M. Calandra, R. Car, C. Cavazzoni, D. Ceresoli, M. Cococcioni, *et al.*, Advanced capabilities for materials modelling with Quantum ESPRESSO, *Journal of Physics: Condensed Matter* **29**, 465901 (2017).

[31] M. J. van Setten, M. Giantomassi, E. Bousquet, M. J. Verstraete, D. R. Hamann, X. Gonze, and G.-M. Rignanese, The PseudoDojo: Training and grading a 85 element optimized norm-conserving pseudopotential table, *Computer Physics Communications* **226**, 39 (2018).

[32] J. P. Perdew, K. Burke, and M. Ernzerhof, Generalized gradient approximation made simple, *Physical Review Letters* **77**, 3865 (1996).

[33] H. J. Monkhorst and J. D. Pack, Special points for Brillouin-zone integrations, *Physical Review B* **13**, 5188 (1976).

[34] J. L. Cheng, N. Vermeulen, and J. E. Sipe, Third order optical nonlinearity of graphene, *New Journal of Physics* **16**, 053014 (2014).

[35] R. W. Boyd, *Nonlinear Optics*, third edition ed. (Academic Press, Burlington, 2008).

[36] D. E. Parker, T. Morimoto, J. Orenstein, and J. E. Moore, Diagrammatic approach to nonlinear optical response with application to weyl semimetals, *Physical Review B* **99**, 1 (2019).

[37] G. Giuliani and G. Vignale, *Quantum Theory of the Electron Liquid* (Cambridge University Press, 2005).

[38] J. P. Carbotte, Dirac cone tilt on interband optical background of type-i and type-ii weyl semimetals, *Physical Review B* **94**, 165111 (2016).

[39] S. Zhu, R. Duan, W. Chen, F. Wang, J. Han, X. Xu, L. Wu, M. Ye, F. Sun, H. Song, S. E. Han, X. Zhao, C. S. Tan, H. Liang, Z. Liu, and Q. J. Wang, Ultrastrong optical harmonic generations in layered platinum disulfide in the mid-infrared, *ACS Nano* **17**, 2148 (2023).

[40] H. Haug and S. W. Koch, *Quantum Theory of the Optical and Electronic Properties of Semiconductors*, 5th ed. (World Scientific Publishing, Singapore, 2009).